OPEN ACCESS



LensingETC: A Tool to Optimize Multifilter Imaging Campaigns of Galaxy-scale Strong Lensing Systems

Anowar J. Shajib^{1,2,10}, Karl Glazebrook^{3,4}, Tania Barone^{3,4}, Geraint F. Lewis⁵, Tucker Jones⁶, Kim-Vy H. Tran^{4,7}, Elizabeth Buckley-Geer^{1,8,2}, Thomas E. Collett⁹, Joshua Frieman^{1,8,2}, and Colin Jacobs^{3,4}, Department of Astronomy & Astrophysics, The University of Chicago, Chicago, IL 60637, USA; ajshajib@uchicago.edu

2 Kavli Institute for Cosmological Physics, University of Chicago, Chicago, IL 60637, USA

3 Centre for Astrophysics and Supercomputing, Swinburne University of Technology, Hawthorn, Victoria 3122, Australia

4 ARC Centre for Excellence in All-Sky Astrophysics in 3D (ASTRO 3D), Australia

5 Sydney Institute for Astronomy, School of Physics, A28, The University of Sydney, NSW 2006, Australia

6 Department of Physics, University of California Davis, 1 Shields Avenue, Davis, CA 95616, USA

7 School of Physics, University of New South Wales, Kensington, Australia

8 Fermi National Accelerator Laboratory, P.O. Box 500, Batavia, IL 60510, USA

9 Institute of Cosmology and Gravitation, University of Portsmouth, Portsmouth PO1 3FX, UK

Received 2022 March 17; revised 2022 September 1; accepted 2022 September 14; published 2022 October 21

Abstract

Imaging data is the principal observable required to use galaxy-scale strong lensing in a multitude of applications in extragalactic astrophysics and cosmology. In this paper, we develop Lensing Exposure Time Calculator (LENSINGETC; https://github.com/ajshajib/LensingETC) to optimize the efficiency of telescope-time usage when planning multifilter imaging campaigns for galaxy-scale strong lenses. This tool simulates realistic data tailored to specified instrument characteristics and then automatically models them to assess the power of the data in constraining lens model parameters. We demonstrate a use case of this tool by optimizing a two-filter observing strategy (in the IR and ultraviolet-visual (UVIS)) within the limited exposure time per system allowed by a Hubble Space Telescope (HST) Snapshot program. We find that higher resolution is more advantageous to gain constraining power on the lensing observables, when there is a trade-off between signal-to-noise ratio and resolution; for example, between the UVIS and IR filters of the HST. We also find that, whereas a point-spread function (PSF) with sub-Nyquist sampling allows the sample mean for a model parameter to be robustly recovered for both galaxy–galaxy and point-source lensing systems, a sub-Nyquist-sampled PSF introduces a larger scatter than a Nyquist-sampled one in the deviation from the ground truth for point-source lens systems.

Unified Astronomy Thesaurus concepts: Strong gravitational lensing (1643); Astronomy software (1855); Astronomical methods (1043)

1. Introduction

Strong gravitational lensing is the phenomenon where a background source is multiply imaged and magnified through the gravitational deflection of photons by a massive deflector in the foreground. Galaxy-scale strong lenses are useful probes of the mass distribution in galaxies at the intermediate redshift $(0.1 \lesssim z \lesssim 1.5)$. Thus, such systems find a multitude of applications in galaxy evolution and cosmology (see, e.g., Treu 2010; Treu & Marshall 2016).

Imaging data are essential for modeling the mass distribution in the deflector, either only from the lensed image positions, and/or by reconstructing the flux distribution of the source galaxy. It can potentially be advantageous to use multiband imaging data in lens modeling instead of single-band data with the same exposure time. If the background galaxies are starforming galaxies with blue clumps, then the lensed arcs will have more structure in the bluer bands, which can potentially provide more constraints for the lens model (e.g., Coe et al. 2010; Dai et al. 2020). However, both the source and the deflector galaxy would have higher signal-to-noise ratio (S/N)

Original content from this work may be used under the terms of the Creative Commons Attribution 4.0 licence. Any further distribution of this work must maintain attribution to the author(s) and the title of the work, journal citation and DOI.

per unit angular area given the same exposure time in redder bands for their typical redshifts and spectral energy distributions (SEDs), i.e., the deflector galaxies typically being red elliptical galaxies and the background galaxies often being blue star-forming galaxies (e.g., Auger et al. 2009; Schmidt et al. 2022). Furthermore, the point-spread function (PSF) differences between the bands can also impact the constraining power of the imaging data. For example, the Hubble Space Telescope (HST) PSF is not Nyquist-sampled—i.e., the FWHM of the PSF does not span at least two pixels—in the infrared (IR) channel; however it does in the ultraviolet-visual (UVIS) channel.

In addition to lensing features, color information of the deflector is often necessary for applying the strong lensing constraints for specific astrophysical applications, e.g., for measuring the stellar mass in deflector galaxies using the stellar population synthesis method to constrain the stellar initial mass function (e.g., Auger et al. 2009; Sonnenfeld et al. 2015). The trade-off between the image resolution and the S/N of the UVIS and IR bands is not obvious, especially given the complex structures of features seen in lensing. Thus, to optimize a multiband observation strategy for efficient usage of limited telescope time, the only way forward is to simulate data to evaluate the achievable uncertainties of key lens model parameters.

In this paper, we describe a new tool for simulating a sample of galaxy-scale strong lenses corresponding to a provided set of

¹⁰ NHFP Einstein Fellow.

instrument specifications, and then to extract the lens model parameter uncertainties from these simulated data (Section 2). Multiple observing scenarios—combinations of exposure times and filters—can be tested in this tool for comparison and selection of the most efficient strategy. Using this, we test various observing strategies to maximize the constraining power of imaging data obtained from one truncated orbit of a HST Snapshot (SNAP) program (Section 3). Furthermore, we investigate any potential systematic impact of the sampling resolution of the PSF in the lens modeling, both for galaxy-galaxy and point-source lens systems (Section 4). Finally, we discuss our results and summarize the paper in Section 5.

2. Description of the Software Program

In this section, we describe our software program Lensing Exposure Time Calculator (LENSINGETC). LENSINGETC uses LENSTRONOMY (Birrer & Amara 2018; Birrer et al. 2021) to simulate and model the mock imaging data. However, the user interface of our program does not require a user to have any experience in using LENSTRONOMY as the user interface only requires specifications of the instrument and the observation. As a result, a user will be able to forecast the lens model parameter uncertainties and optimize the observing strategies using our software program with minimal setup time (~30 minutes) required. We describe the simulation of mock lenses in Section 2.1 and the modeling of the mock lenses in Section 2.2.

2.1. Simulating Mock Lens Systems

2.1.1. Instrument Specifications

The simulation module requires specifications of the following instrument/image properties for each of the adopted filters: read noise, CCD gain, sky brightness, magnitude zeropoint, pixel scale, number of pixels in the simulated image, PSF (can be supersampled or nonsupersampled), and cosmic-ray event rate (optional). Additionally, a set of observing strategies can be provided to the simulation that specifies the number of exposures per filter and the integration time of a single exposure. If the user chooses to exclude cosmic rays in the simulation, specifying the number of multiple exposures is still recommended so that the read noise from each single exposure can be appropriately added to the total noise level. The user needs to already account for instrument overhead before providing the exposure times to LENSINGETC. If a cosmic-ray event rate is provided, the different exposures have different simulated realizations of cosmic-ray-hit pixels, and the total exposure time per pixel is computed by disregarding the cosmic-ray-hit pixels in the different exposures. Then, Poisson noise is added to the simulated images based on the effective exposure time per pixel, and background noise and read noise are also applied to the final simulated image.

2.1.2. Lens Galaxy Mass and Light

We use an elliptical power-law mass profile to describe the mass distribution of the lens galaxy (Barkana 1998; Tessore & Benton Metcalf 2015). The convergence—i.e., the surface mass density normalized by the critical density of lensing—of this

Table 1
Lens Galaxy Model Parameter Specifications

Parameter	Description	Distribution
${\gamma}$	Power-law exponent	U(1.9, 2.1)
$ heta_{ m E}$	Einstein radius	<i>U</i> (1."2, 1."6)
$q_{ m m}$	Mass axis ratio	U(0.7, 0.9)
$\varphi_{\mathbf{m}}$	Mass position angle	$\mathcal{U}(-90 \deg, 90 \deg)$
γ_1	External shear	$\mathcal{U}(-0.08, 0.08)$
γ_2	External shear	$\mathcal{U}(-0.08, 0.08)$
$q_{ m L}$	Light axis ratio	Joint with $q_{ m m}$
$arphi_{ m L}$	Light position angle	Joint with $arphi_{ m m}$

Note. γ_1 and γ_2 are external shear parameters in the Cartesian coordinate system that are related to the external shear magnitude $\gamma_{\rm ext}$ and $\varphi_{\rm ext}$ as $\gamma_1 \equiv \gamma_{\rm ext} \cos(2\varphi)$ and $\gamma_2 \equiv \gamma_{\rm ext} \sin(2\varphi)$. The function $\mathcal{U}(a,b)$ denotes a uniform distribution within a and b.

mass profile is given by

$$\kappa_{\rm PL}(x,y) \equiv \frac{3-\gamma}{2} \left[\frac{\theta_{\rm E}}{\sqrt{q_{\rm m}x^2 + y^2/q_{\rm m}}} \right]^{\gamma-1},\tag{1}$$

where γ is the logarithmic slope, $\theta_{\rm E}$ is the Einstein radius, and $q_{\rm m}$ is the axis ratio. We also add external shear in the lens mass model. We provide the adopted distributions of the lens model parameters in Table 1. We use the Sérsic function to describe the light distribution of the lens galaxy, which is given by

$$I(x, y) \equiv I_{\text{eff}} \exp \left[-b_n \left\{ \left(\frac{\sqrt{q_L x^2 + y^2/q_L}}{R_{\text{eff}}} \right)^{1/n_s} - 1 \right\} \right], (2)$$

where $R_{\rm eff}$ is the effective radius along the intermediate axis, $I_{\rm eff}$ is the amplitude at $R_{\rm eff}$, and $n_{\rm s}$ is the Sérsic index (Sérsic 1968). Additionally, b_n is a normalizing factor so that $R_{\rm eff}$ becomes the half-light radius. We fix $n_{\rm s}=4$, which is a typical value for massive elliptical galaxies (e.g., Tasca & White 2011), as massive ellipticals are the most common type of deflector galaxies in galaxy-scale strong lenses (e.g., Bolton et al. 2006; Gavazzi et al. 2012). The total apparent magnitude of the lens galaxy can be provided to the simulation module, which is then converted to $I_{\rm eff}$ in the flux unit of electron s⁻¹.

2.1.3. Source Galaxy Light

We use light profiles of real spiral and disky galaxies from the HST legacy imaging as the source galaxy light distribution. We select 1117 spiral and disky galaxies from the Galaxy Zoo catalog of 120,000 galaxies that are morphologically classified through crowdsourcing (Willett et al. 2017). To select spiral and disky galaxies, we use these criteria: t01_smooth_or_ features_a01_smooth_flag = True or t01_smooth_ or_features_a02_features_or_disk_flag = True, t06_odd_a02_no_weighted_fraction > 0.85 (for definitions of the criteria; see Willett et al. 2017). The selected images are from either of the surveys: the All Wavelength Extended Groth Strip International Survey (AEGIS; Georgakakis et al. 2007), Galaxy Evolution from Morphologies and SEDs (GEMS; Caldwell et al. 2008), and the Great Observatories Origins Deep Survey (GOODS; Giavalisco et al. 2004). The photometric redshifts of the selected galaxies range from

¹¹ An easy-to-follow example is provided as a JUPYTER notebook in the GitHub repository: https://github.com/ajshajib/LensingETC.

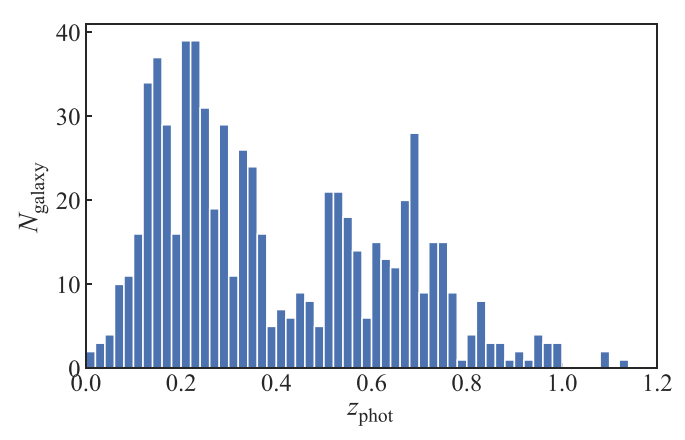


Figure 1. Distribution of photometric redshifts of the 699 spiral and disky galaxies selected from the Galaxy Zoo catalog.

0.01 to 1.33 (see Figure 1). Although typical source galaxies of strong lensing systems have a mean redshift of ~ 2 , we only use the morphologies of the selected galaxies in the simulation and not their colors, which needs to be set by the user appropriately. Thus, the redshift distribution of these galaxies is unimportant for the purpose of our software program.

Using the R.A. and decl. of the selected galaxies, we retrieve $5'' \times 5''$ cutouts from the HST legacy archive. These images are from the ACS camera in the F606W filter. Based on visual inspection of the downloaded images, we further remove images with noticeable cosmic-ray hits, systems near the edge of the cutout, systems that are too faint or too small (i.e., only covering $\lesssim 10$ pixels), systems with very irregular shape or light distribution not resembling a spiral or disky galaxy, and systems that are too large extending beyond the cutout size. After this quality control procedure, we end up with 699 images cutouts of disky and spiral galaxies (for a few examples, see Figure 2).

We extract the morphological information of the source galaxies by fitting a basis set of shapelets—i.e., 2D dimensionless Gauss–Hermite polynomials—to these galaxy light profiles (Refregier 2003). The 1D shapelet function, i.e., the dimensionless Gauss–Hermite polynomial, is given by

$$B_n(x; \beta) \equiv \beta^{-\frac{1}{2}} [2^n \pi^{\frac{1}{2}} n!]^{-\frac{1}{2}} H_n(\beta^{-1} x) \exp\left(-\frac{x^2}{2\beta^2}\right), \quad (3)$$

where β is a scale parameter, and H_n is the Hermite polynomial of order n. In 2D, the shapelet function with order (n_1, n_2) is given by

$$B_{n_1,n_2}(x, y; \beta) \equiv B_{n_1}(x; \beta)B_{n_2}(y; \beta).$$
 (4)

These functions are orthogonal; thus they form a linearly independent basis set. Extracting the morphological information in the parametric form of the shapelets allows us to easily scale the sizes of these galaxies in our simulation. We choose the highest polynomial order $n_{\rm max}=50$. Thus, the total number of shapelet components (i.e., the number of free linear parameters) in the basis set is $(n_{\rm max}+1)(n_{\rm max}+2)/2=1326$.

We select the most appropriate shapelet scale parameter β for this fitting by finding the minimum χ^2 fit out of multiple fits with gradually increasing β values from 0."025 to 1" with a uniform step size of 0."025. Once the best-fit amplitudes of the 1326 shapelet components are obtained with an optimal β parameter, then the β parameter can be randomly set in the simulation to enlarge or shrink the size of the galaxy while retaining the morphological structure of the galaxy, which is set by the relative amplitudes of the shapelet components. For each simulated lensing system created in this paper, we randomly sample β from $\mathcal{U}(0.1, 0.2)$, where this size corresponds to the unlensed size on the source plane. Figure 2 illustrates some examples of the real HST images of the source galaxies and their shapelet-based reconstructions. For ease of use, the user can select particular galaxies to use as the source from our list of 699 galaxies instead of relying on random selection, or can directly provide shapelet coefficients if other galaxy morphologies not included in our list are desired.

Additionally, a point source can be added at the center of the source galaxy to simulate the presence of a quasar or a supernova. Although a supernova may not necessarily be at the center of the host galaxy, the exact position of the supernova within the galaxy does not impact the statistical constraining power of the imaging data at the sample level given the random positioning of the source galaxy with respect to the caustic curve. The user is required to provide distributions of the total magnitudes corresponding to lens galaxy, source galaxy, and the point source for each adopted filter.¹³

2.2. Modeling of the Simulated Lenses

Our software program automatically sets up the lens model specifications to optimize the model with LENSTRONOMY. The modeling of the simulated images is performed in the same way as done for real imaging data (e.g., Shajib et al. 2019, 2021). The mass and light profiles that are optimized in the lens modeling have the same parameterization as in Sections 2.1.2 and 2.1.3. The model parameter uncertainties are obtained from Markov Chain Monte Carlo (MCMC) sampling using the software EMCEE (Goodman & Weare 2010; Foreman-Mackey et al. 2013). As we allow the lens galaxy's light model parameters as free parameters instead of pre-subtracting a separately fitted light profile from the data, the potential systematic arising from the latter approach is marginalized over and the associated uncertainty is included in the extracted uncertainty for the lens mass model parameters. If multiple filters are specified for an observing strategy, then all the filters are simultaneously modeled through a joint likelihood function.

In the modeling, the user can choose to provide a different or lower-resolution PSF than the one used for the simulations for any of the specified filters to mimic a real-world modeling scenario. The user can also choose different $n_{\rm max}$ parameters in the simulation and modeling, as usually $n_{\rm max} \leq 10$ is sufficient to model lensing systems with the resolution of current highend facilities such as the HST (e.g., Shajib et al. 2019).

3. Optimal Observing Strategy for HST SNAP Program

Here, we perform a comparison test between different observing strategies of galaxy-galaxy lens systems for the HST

¹² Although LENSTRONOMY allows using a pixelated flux profile as the source galaxy light distribution through the `INTERPOL'' profile (Wagner-Carena et al. 2022), we find the shapelet-based description to be more advantageous due to its flexibility in rescaling the galaxy size and in tuning the degree of clumpiness in the simulation.

 $[\]overline{^{13}}$ For some example values to use as the magnitude distributions that are consistent with those of the lens sample presented by Shajib et al. (2019), see Sections 3 and 4.

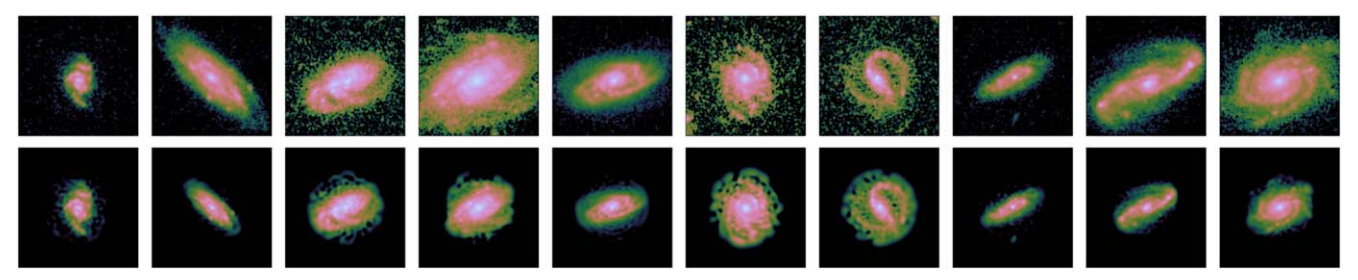


Figure 2. Top row: HST legacy imaging of spiral galaxies from the Galaxy Zoo catalog. Bottom row: Reconstruction of the light distribution based on a basis set of shapelets (i.e., 2D Gauss-Hermite polynomial) with maximum polynomial order $n_{\text{max}} = 50$. The shapelet-based reconstructions are rescaled to the same characteristic size.

SNAP program GO-16773 that aims to image strong lensing systems discovered in Dark Energy Survey data (Jacobs et al. 2019a, 2019b). The observations in a SNAP program are limited to \lesssim 45 minutes including overheads, as targets from these programs are used to fill in scheduling gaps in between targets from General Observer (GO) programs.

3.1. Test Setup

We choose two filters in our setup: F140W (IR) and F200LP (UVIS). Although deflector galaxies—which are typically red ellipticals—are brighter in the IR band, the source galaxies—which are typically star-forming galaxies—have more structure from the star-forming regions in the bluer UVIS band (see Figure 3). We choose these two filters, because they are wide filters that allow maximize the collected photons and thus the S/N given the exposure time constrain of a SNAP program. Although the PSF in wide filters has relatively stronger color dependence than the narrow ones, we find that this color dependence is insignificant in the context of lens modeling (see also Shajib et al. 2021).

We choose six cases of exposure time allocation that range from allocating the maximum time for the F140W filter to allocating the maximum time for the F200LP filter (see Table 2). We have already accounted for the instrument overheads using the HST Astronomer's Proposal Tool (APT) and chosen the exposure sequences so as to minimize the overhead within the observing time limit.

We choose the pixel sizes 0.08 for the F140W filter and 0.04 for the F200LP filter to mimic the pixel scales of drizzled images (Shajib et al. 2019). For the F140W filter, we use a supersampled PSF with resolution factor of 3 in the simulation, but for modeling we use a nonsupersampled PSF. For the F200LP filter, the same nonsupersampled PSF is used for both simulation and modeling. However, the UVIS pixel size of 0.04 in the PSF already Nyquist samples the HST PSF. For both simulation and modeling, we choose $n_{\rm max} = 4$ and $n_{\rm max} = 8$ for the F140W and F200LP filters, respectively.

For simulating the images, we take the shapelets up to an order of 4 or 8 for the F140W or the F200LP filters, respectively, out of all the shapelets up to an order of 50 that were extracted in Section 2.1.3. For an average $\beta=0.^{\prime\prime}15$ and a typical magnification of $\sim\!4$ (e.g., the median magnification for the sample from Schmidt et al. 2022), the adopted $n_{\rm max}$ values allow to have structural features in the source galaxy with image-plane size $\sim\!4\times0.^{\prime\prime}15\times2.355/(2n_{\rm max}+1)$, which are $\sim\!0.^{\prime\prime}157$ and $\sim\!0.^{\prime\prime}083$ for the F140W and F200LP filters, respectively. The factor of 2.355 makes the size definition equivalent to the FWHM of a Gaussian function. The PSF

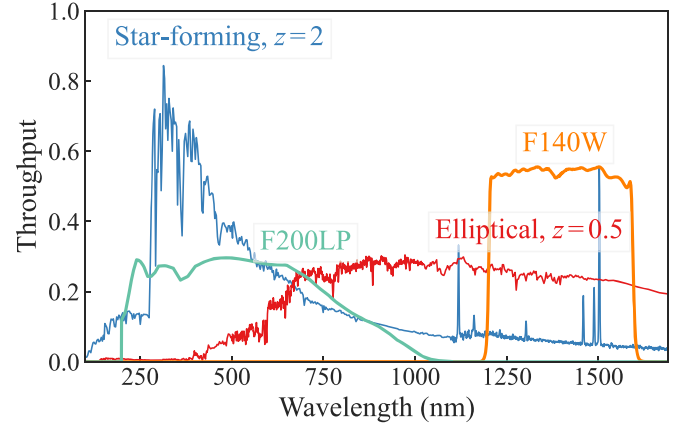


Figure 3. Throughput of the F200LP (emerald line) and F140W (orange line) filters of the HST WFC3. The spectral energy distributions of a star-forming galaxy (blue line) at z=2 and an elliptical galaxy (red line) at z=0.5 are also illustrated with arbitrary amplitude scaling. Each of the two adopted filters maximizes the relative contribution from either the deflector or the source galaxy to the total light.

 Table 2

 Different Observing Strategies for a HST SNAP Program in our Test Setup

Case	F140W Exposure Time (s)	F200LP Exposure Time (s)	Total SNAP Visit Time including Overheads (s)
1	4 × 350	•••	1905
2	3×300	1×300	1773
3	2×300	2×300	1881
4	3×200	2×300	1901
5	1×300	2×450	1861
6	•••	2 × 650	1819

FWHMs for the F140W and F200LP filters are 0."144 and 0."083, respectively. Thus, the chosen n_{max} values are sufficient to have structures in the source galaxy down to the PSF resolution limit. In the simulation, we use the following magnitude and color distributions that are consistent with the lens systems presented in Shajib et al. (2019):

- 1. Lens galaxy: $m_{\rm F140W} \sim \mathcal{N}(18.5, 0.5) \ m_{\rm F200LP} m_{\rm F140W} \sim \mathcal{N}(2.7, 0.2),$
- 2. Unlensed source galaxy: $m_{\rm F140W} \sim \mathcal{N}(20.80, 0.08)$ $m_{\rm F200LP} - m_{\rm F140W} \sim \mathcal{N}(2.0, 0.2)$.

We add the the effect of cosmic rays in the simulated exposures. We set the cosmic-ray event rate to be $1.2\times10^{-4}~\text{s}^{-1}~\text{arcsec}^{-2}$ in the F140W filter and $2.4\times10^{-4}~\text{s}^{-1}~\text{arcsec}^{-2}$ in the F200LP

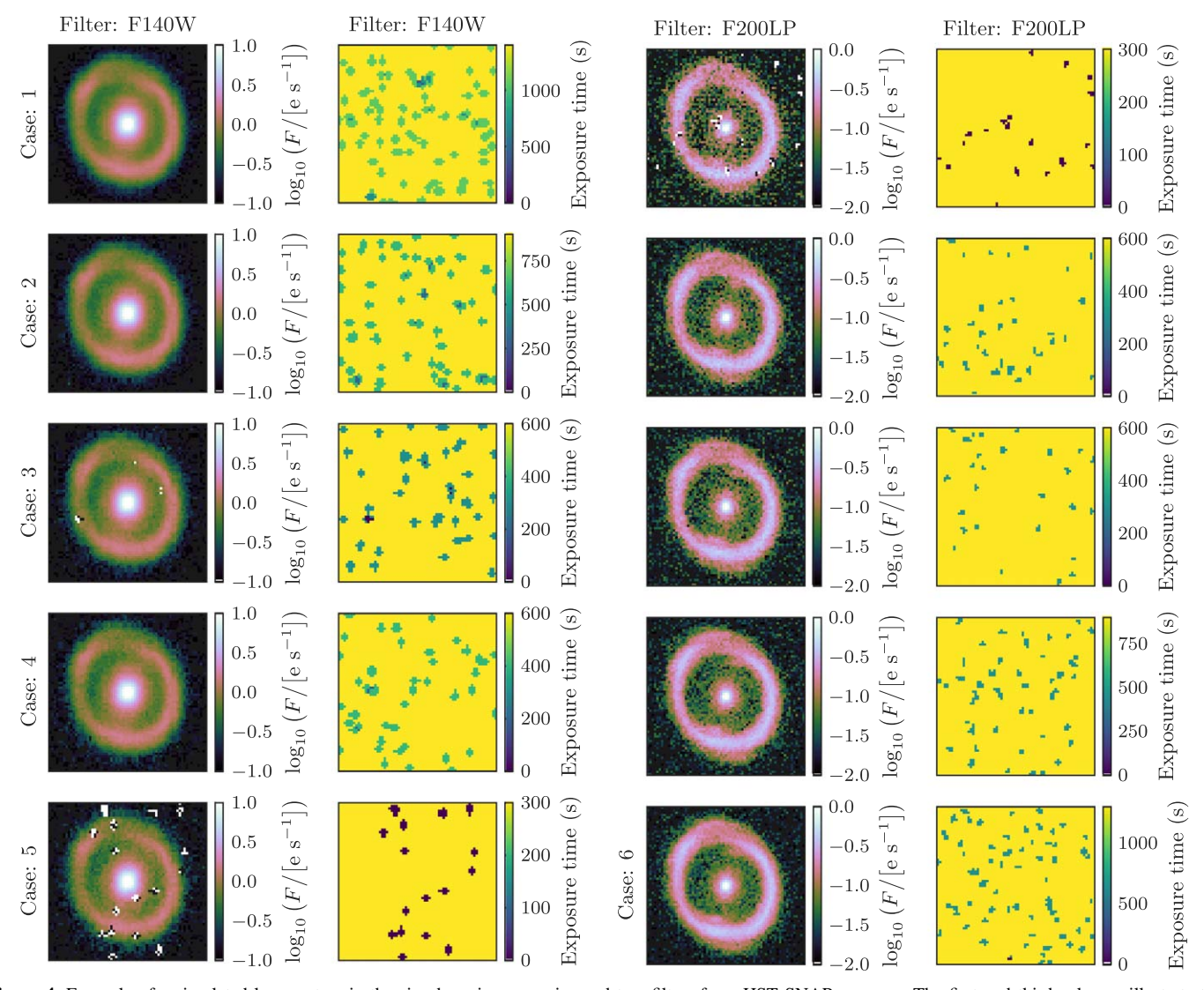


Figure 4. Example of a simulated lens system in the six observing scenarios and two filters for a HST SNAP program. The first and third columns illustrate the simulated imaging data, and the second and fourth columns illustrate the exposure time map after accounting for the impact of cosmic-ray hits. A montage of the full sample of 20 lenses is given in Figure 7.

filter. These values are estimated by counting cosmic-ray hits within a $10'' \times 10''$ area in real HST exposures. The event rate in the F140W filter is smaller than the F200LP filter, because not every cosmic-ray hit is catastrophic in the IR detector as nondestructive readout is possible in this detector. However, the event rate in the F140W filter accounts for the presence of random dead or hot pixels in the exposures.

We simulate 20 lensing systems for each of the six observing scenarios and obtain the model parameter uncertainties for each case from MCMC chains. The 20 simulated lenses provide a sufficiently large sample to distinguish between the observing strategies considered here. Figure 4 illustrates several examples of the simulated images and the corresponding exposure maps with random realizations of cosmic-ray hits.

3.2. Result

In Figure 5, we compare the posterior uncertainties of the Einstein radius $\theta_{\rm E}$ and the power-law slope γ between the observing strategies. We choose these two parameters for comparing the constraining power of the data for different strategies, as they are central lens model parameters

pertaining to the deflector galaxy. ¹⁴ We find that the constraining power of the data increases for both $\theta_{\rm E}$ and γ as a greater fraction of a fixed time is allocated for the higher-resolution UVIS filter. In other words, for realistic magnitudes and colors of typical deflector and source galaxies, higher image resolution is more advantageous than higher S/N to constrain the lens models.

Based on this result, we adopt Case 4 as the observing strategy for our HST SNAP program GO-16773. The science cases of this program require measured colors of the deflector and the source galaxies; thus Cases 1 and 6 are not considered as both of these use only a single filter. We only included these cases in our experiment to illustrate the edge cases. Although both Cases 3 and 4 allocate the same total exposure time to the F140W filter, Case 4 allows for a more artifact-free drizzled

¹⁴ Although the primary direct observables in the imaging data are the Einstein radius θ_E and the quantity $\theta_E \alpha''(\theta_E)/[1-\kappa(\theta_E)]$ with α'' being the double derivative of the deflection angle (Kochanek 2020; Birrer 2021), for the power-law model the latter quantity simply becomes $\gamma-2$. As we use a power-law model as the ground truth to simulate the data, adopting γ as the observable quantity serves the purpose of assessing the constraining power of the data on the lensing mass distribution.

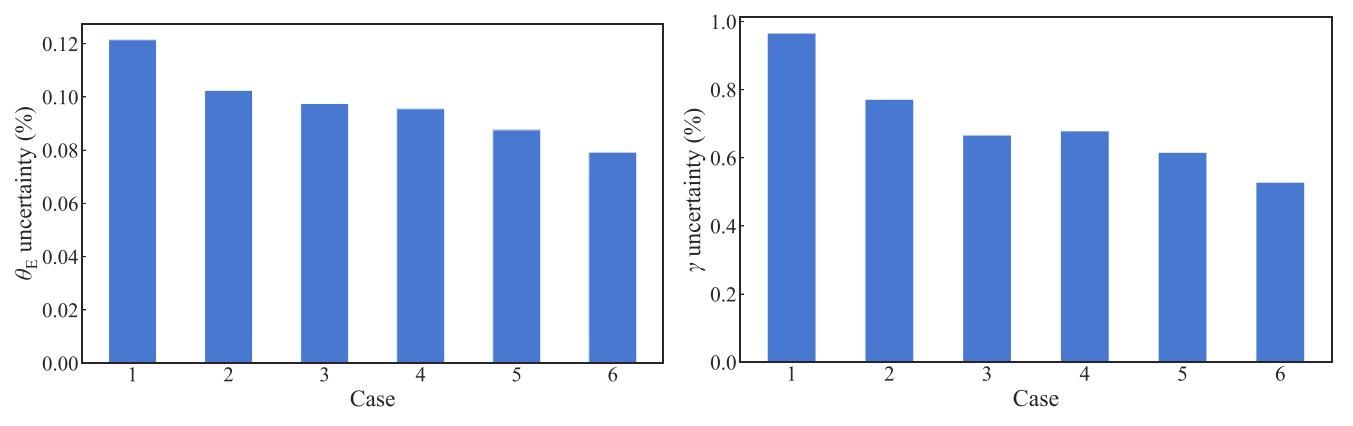


Figure 5. Comparison of parameter uncertainties between the six observing strategies or cases for HST SNAP program: for Einstein radius $\theta_{\rm E}$ in the left-hand panel, and for the logarithmic slope parameter γ in the right-hand panel. For each observing strategy or case, the illustrated parameter uncertainty is the mean of the individual uncertainties from 20 lens systems. The six strategies distribute \sim 2000 s of total observing time of one HST truncated orbit between two filters: from allocating all the time for the F140W filter in Case 1 to allocating all the time for the F200LP filter in Case 6. As the F200LP band allows for higher resolution than the F140W band, a higher image resolution is more constraining for lens models than a higher S/N for typical strong lensing systems.

image by dividing the total exposure time into three exposures instead of two (see Figure 4). Although Case 5 provides better constraints than Case 4, Case 5 is not chosen for the same reason above, as the cosmic-ray-hit and dead pixels lead to considerably degraded IR photometry, which is not desirable to meet the requirements of the science cases.

4. Impact of PSF Sampling in Modeling

In this section, we perform a test using LENSINGETC on the impact of the PSF sampling resolution in lens modeling. A supersampled PSF, or even a Nyquist-sampled PSF, is not always available a priori for lens modeling. For systems with point sources, the PSF is usually reconstructed from an initial estimate based upon nearby stars (Chen et al. 2016; Birrer et al. 2019). For galaxy–galaxy strong lenses, an estimate of the PSF—either from nearby stars or from simulation (e.g., TINYTIM for HST)—is used for modeling. The PSF is not Nyquist-sampled in the IR channel of HST, for example. Here, we investigate whether such suboptimally sampled PSFs systematically impact the lens model posterior. As the PSF is integral in lens modeling to extract the lensing information, this investigation will determine if additional procedures are necessary to obtain supersampled and accurate PSFs as part of an imaging program.

4.1. Test Setup

We choose four scenarios that are combinations of galaxy-galaxy and point-source lens systems, and supersampled and nonsupersampled PSFs (see Table 3).

For all these scenarios, we only simulate single-filter images with the instrument specifications corresponding to the HST Wide-Field Camera 3 (WFC3) F140W filter. A supersampled PSF with a resolution factor of 3 is used to simulated the images in all the scenarios. We adopt the total exposure time of $8\times275\,\mathrm{s}$ per system (achievable from one orbit of an HST GO program; e.g., Shajib et al. 2019). For the scenarios with nonsupersampled PSFs for modeling, we degrade the supersampled PSF through binning to match the PSF pixel size with the imaging pixel size. We adopt a 50% flux uncertainty for the PSFs used in modeling the point-source lens systems, which is a realistic uncertainty level as found in the experiment done by Ding et al. (2021). The simulated point-source lens systems have the same background galaxy as in the simulated galaxy–galaxy lens systems, and we add a point source

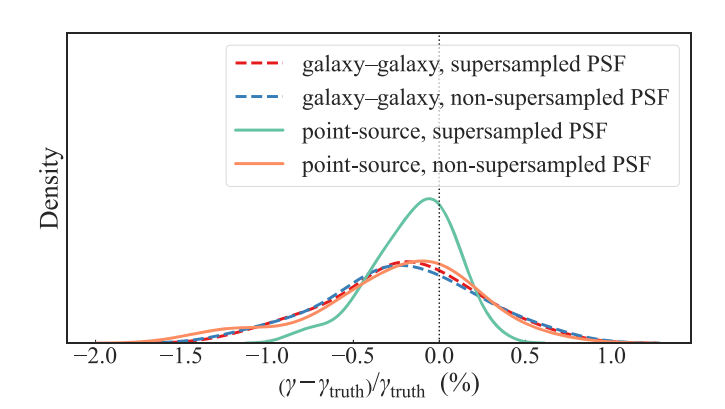


Figure 6. Deviations in power-law slope parameter γ for galaxy–galaxy and point-source lenses modeled with and without supersampled PSF. The illustrated distributions correspond to kernel density estimates from 20 lens systems for each case. For galaxy–galaxy lens systems (dashed lines), the PSF supersampling does not noticeably impact the distribution of deviations. However, for point-source lenses, modeling with the nonsupersampled PSF creates a larger scatter than that with the supersampled PSF. In all cases, the mean deviation at the sample level is within 0.25% from zero.

Table 3
Test Scenarios with Different Lens System Types and PSF Supersampling

Scenario	System Type	PSF
1	galaxy–galaxy lens system	supersampled
2	galaxy–galaxy lens system	nonsupersampled
3	point-source lens system	supersampled
4	point-source lens system	nonsupersampled

at the center of the background galaxy with an unlensed magnitude sampled from $m_{\rm F140W} \sim \mathcal{U}(20,\,21)$. The deflector and host galaxy magnitude distributions are the same as in Section 3. We simulate 20 lens systems for each scenario. For the sample of point-source lenses, we have 5 quadruple-image systems and 15 double-image systems out of the 20 from random positioning of the source centroid on the source plane.

4.2. Result

Figure 6 compares the systematic deviations in the modeled γ parameter in the four test scenarios. For all the

scenarios, the mean deviation at the sample level is within 0.25% from zero. For galaxy–galaxy lens systems, there is no significant difference in the distributions of the deviations between the scenarios having supersampled and nonsupersampled PSFs. However, for systems with point sources, the case with the nonsupersampled PSF has a larger scatter in the γ parameter than the case with the supersampled PSF. This is due to the fact that the accuracy of the point-source positioning depends on the PSF resolution and the positions of the modeled point-source impact the lens model posterior.

5. Discussion and Summary

In this paper, we present a simulation tool, LENSINGETC, to optimize the observation strategies of galaxy-scale strong lensing systems to achieve maximum constraining power from the imaging data. This tool is built on the lens modeling software program LENSTRONOMY. We provide an easily accessible user interface that does not require any prior experience in using LENSTRONOMY. The user only needs to provide instrument and observation specifications, and apparent magnitude distributions of the deflector and the lensed objects. Our tool then simulates mock imaging data and performs lens modeling with the mock data to obtain the model parameter uncertainties. Thus, our tool allows an investigator to perform the optimization with minimal setup time (≤ 30 minutes) required. This tool can be used to experiment with both galaxy-galaxy and point-source lens systems. For simulated imaging data with two filters, running the MCMC chain to obtain the model posterior requires \sim 2 CPU hours for each combination of lens and observing case. 15 Thus, for typical imaging programs with \sim 5 observing cases to optimize from—such as the one performed in Section 3—the optimization procedure takes a time of the order of days to run all the MCMC chains for the combinations of simulated lenses and

Although our tool is built for galaxy-scale strong lensing systems, the results can be qualitatively generalized to groupscale and cluster-scale strong lensing systems. The lensing observables captured in the lensed arcs within the imaging data can be generalized for all cases of strong lensing and even up to the regime of weak lensing (Birrer 2021). Our tool uses the same lens model to simulate and fit the imaging data, the model posterior only captures the statistical uncertainty without any additional modeling systematics. Thus, the statistical constraining power of the local lensing observables contained in the lensed arcs can be generalized to group and cluster scales for a similar range of lensing magnification and source magnitude. However, specific systematics that may potentially arise from particular modeling methods used for group-scale and clusterscale lenses are not captured in the results of our tool; thus these systematics may be required to be considered before making quantitative forecasts using the results from the tool presented in this paper.

We use our tool to optimize the observation strategy for an HST SNAP program with $\lesssim 2000\,\mathrm{s}$ as the total observing time per lens system including overhead. We find that the higher imaging resolution of the HST UVIS channel provides more constraining power than the higher S/N achievable with the IR channel. Thus, the resolved structure

in the lensed arcs deliver more lensing information to constrain the lens model than a higher S/N in the flux distribution of the lensed arcs.

We furthermore test the importance of PSF sampling resolution in the robust estimation of the lens model parameters. For both galaxy–galaxy and point-source lens systems, the mean deviation of the power-law slope γ at the sample level is within 0.25% from zero for both optimal and nonoptimal (i.e., sub-Nyquist) PSF sampling. This deviation is negligible given the typical uncertainty achieved with imaging data from current instruments is $\sim 2\%-5\%$ (Shajib et al. 2019, 2021; Schmidt et al. 2022) We find that the PSF supersampling resolution has no impact in the modeling galaxy–galaxy strong lensing systems. This is consistent with Shajib et al. (2021), who find no significant difference from using multiple simulated and empirical PSFs with varying SED and resolution in modeling HST images of galaxy–galaxy lenses.

However, we find that a sub-Nyquist-sampled PSF creates larger scatter in the deviation of the recovered γ parameter from the ground truth than a higher-resolution PSF above the Nyquist limit. Such a large scatter is consistent with Shajib et al. (2022), who find that the PSF resolution can significantly $(\sim 4\sigma)$ shift the best-fit γ parameter, and a supersampled PSF leads to consistent lens model posteriors even if different modeling softwares are used. Therefore, supersampled PSFs are recommended in lens modeling applications such as the time-delay cosmography that is strongly sensitive to the γ parameter and typically uses one lens system at a time. Additional observing procedures, e.g., observing nearby stars or choosing systems with a larger number of nearby stars to fit within the same HST frame, may be necessary to create a robust initial PSF estimate with supersampled resolution. However, once a large sample of lens systems are considered the scatter in the γ parameter will be averaged out to bring the sample mean closer to the ground truth, i.e., the systematics from sub-Nyquist-sampled PSFs can be mitigated at the sample level.

We thank Simon Birrer and the anonymous referee for helpful comments that improved this manuscript. Support for this work was provided by NASA through the NASA Hubble Fellowship grant HST-HF2-51492 awarded to A.J.S. by the Space Telescope Science Institute, which is operated by the Association of Universities for Research in Astronomy, Inc., for NASA, under contract NAS5-26555. T.J. gratefully acknowledges funding support from the Gordon and Betty Moore Foundation through Grant GBMF8549, from NASA through grant HST-GO-16773.002-A, from the National Science Foundation through grant AST-2108515, and from a Dean's Faculty Fellowship. T.E.C. is funded by a Royal Society University Research Fellowship and the European Research Council (ERC) under the European Union's Horizon 2020 research and innovation program (LensEra: grant agreement No. 945536).

Facilities: HST, MAST.

Software: LENSTRONOMY (Birrer & Amara 2018; Birrer et al. 2021), EMCEE (Foreman-Mackey et al. 2013), NUMPY (Oliphant 2015), SCIPY (Jones et al. 2001), MATPLOTLIB (Hunter 2007), SEABORN (Waskom et al. 2014).

¹⁵ We performed the MCMC sampling on a system with AMD Ryzen 7 3700X 8-core processor with a clock speed of 3.6 GHz.

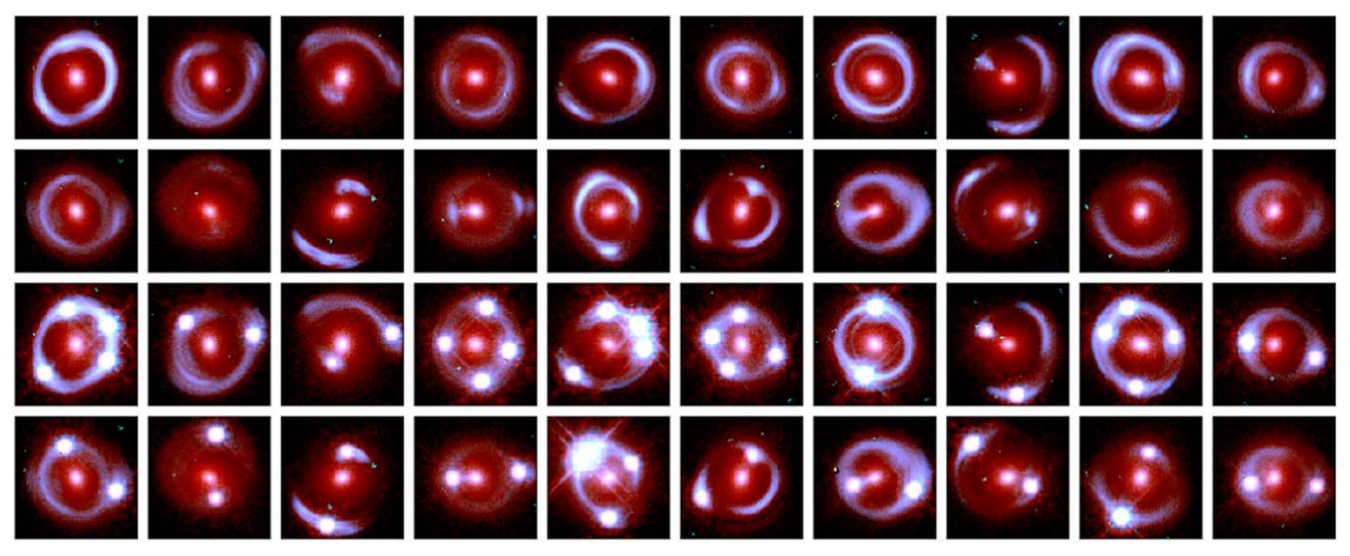


Figure 7. False-color composite images of the simulated galaxy-galaxy (tow 2 rows) and point-source (bottom 2 rows) lens systems from Sections 3 and 4. The RGB images are created from a weighted combination of monochrome images from the F140W and F200LP filters.

Appendix Simulated Lenses

In Figure 7, we illustrate false-color composites of all the simulated galaxy–galaxy and point-source lenses simulated in Sections 3 and 4.

ORCID iDs

Anowar J. Shajib https://orcid.org/0000-0002-5558-888X Karl Glazebrook https://orcid.org/0000-0002-3254-9044 Tania Barone https://orcid.org/0000-0002-2784-564X Geraint F. Lewis https://orcid.org/0000-0003-3081-9319 Tucker Jones https://orcid.org/0000-0001-5860-3419 Kim-Vy H. Tran https://orcid.org/0000-0001-9208-2143 Elizabeth Buckley-Geer https://orcid.org/0000-0002-3304-0733

Thomas E. Collett https://orcid.org/0000-0001-5564-3140
Joshua Frieman https://orcid.org/0000-0003-4079-3263
Colin Jacobs https://orcid.org/0000-0003-4239-4055

References

Auger, M. W., Treu, T., Bolton, A. S., et al. 2009, ApJ, 705, 1099
Barkana, R. 1998, ApJ, 502, 531
Birrer, S. 2021, ApJ, 919, 38
Birrer, S., & Amara, A. 2018, PDU, 22, 189
Birrer, S., Shajib, A., Gilman, D., et al. 2021, JOSS, 6, 3283
Birrer, S., Treu, T., Rusu, C. E., et al. 2019, MNRAS, 484, 4726
Bolton, A. S., Burles, S., Koopmans, L. V. E., Treu, T., & Moustakas, L. A. 2006, ApJ, 638, 703
Caldwell, J. A. R., McIntosh, D. H., Rix, H.-W., et al. 2008, ApJS, 174, 136
Chen, G. C.-F., Suyu, S. H., Wong, K. C., et al. 2016, MNRAS, 462, 3457

Coe, D., Benitez, N., Broadhurst, T., & Moustakas, L. A. 2010, ApJ, 723, 1678 Dai, L., Kaurov, A. A., Sharon, K., et al. 2020, MNRAS, 495, 3192 Ding, X., Liao, K., Birrer, S., et al. 2021, MNRAS, 504, 5621 Foreman-Mackey, D., Hogg, D. W., Lang, D., & Goodman, J. 2013, PASP, 125, 306 Gavazzi, R., Treu, T., Marshall, P. J., Brault, F., & Ruff, A. 2012, ApJ, 761, 170 Georgakakis, A., Nandra, K., Laird, E. S., et al. 2007, ApJL, 660, L15 Giavalisco, M., Ferguson, H. C., Koekemoer, A. M., et al. 2004, ApJL, Goodman, J., & Weare, J. 2010, CAMCS, 5, 65 Hunter, J. D. 2007, CSE, 9, 90 Jacobs, C., Collett, T., Glazebrook, K., et al. 2019a, MNRAS, 484, 5330 Jacobs, C., Collett, T., Glazebrook, K., et al. 2019b, ApJS, 243, 17 Jones, E., Oliphant, T., & Peterson, P. 2001, SciPy: Open Source Scientific Tools for Python, http://www.scipy.org/ Kochanek, C. S. 2020, MNRAS, 493, 1725 Oliphant, T. E. 2015, Guide to NumPy (2nd ed.; USA: CreateSpace Independent Publishing Platform), https://numpy.org/ Refregier, A. 2003, MNRAS, 338, 35 Schmidt, T., Treu, T., Birrer, S., et al. 2022, arXiv:2206.04696 Sérsic, J. L. 1968, Atlas de Galaxias Australes (Cordoba: Observatorio Shajib, A. J., Birrer, S., Treu, T., et al. 2019, MNRAS, 483, 5649 Shajib, A. J, Treu, T., Birrer, S., & Sonnenfeld, A. 2021, MNRAS, 503, 2380 Shajib, A. J., Wong, K. C., Birrer, S., et al. 2022, arXiv:2202.11101 Sonnenfeld, A., Treu, T., Marshall, P. J., et al. 2015, ApJ, 800, 94 Tasca, L. A. M., & White, S. D. M. 2011, A&A, 530, A106 Tessore, N., & Benton Metcalf, R. 2015, A&A, 580, A79 Treu, T. 2010, ARA&A, 48, 87 Treu, T., & Marshall, P. J. 2016, A&ARv, 24, 11 Wagner-Carena, S., Aalbers, J., Birrer, S., et al. 2022, arXiv:2203.00690 Waskom, M., Botvinnik, O., Hobson, P., et al. 2014, seaborn: v0.5.0 (November 2014), Zenodo, doi:10.5281/zenodo.12710 Willett, K. W., Galloway, M. A., Bamford, S. P., et al. 2017, MNRAS, 464, 4176